nature physics

LETTERS

https://doi.org/10.1038/s41567-018-0080-5

Ultrafast preparation and detection of ring currents in single atoms

Sebastian Eckart[1*], Maksim Kunitski[1], Martin Richter[1], Alexander Hartung[1], Jonas Rist[1], Florian Trinter[1], Kilian Fehre[1], Nikolai Schlott[1], Kevin Henrichs[1], Lothar Ph. H. Schmidt[1], Till Jahnke[1], Markus Schöffler[1], Kunlong Liu[2], Ingo Barth[2], Jivesh Kaushal[3], Felipe Morales[3], Misha Ivanov[3], Olga Smirnova[3,4] and Reinhard Dörner[1*]

Quantum particles can penetrate potential barriers by tunnelling[1]. If that barrier is rotating, the tunnelling process is modified[2,3]. This is typical for electrons in atoms, molecules or solids exposed to strong circularly polarized laser pulses[4–6]. Here we measure how the transmission probability through a rotating tunnel depends on the sign of the magnetic quantum number *m* of the electron and thus on the initial direction of rotation of its quantum phase. We further show that our findings agree with a semiclassical picture, in which the electron keeps part of that rotary motion on its way through the tunnel by measuring *m*-dependent modification of the electron emission pattern. These findings are relevant for attosecond metrology as well as for interpretation of strong-field electron emission from atoms and molecules[7–14] and directly demonstrate the creation of ring currents in bound states of ions with attosecond precision. In solids, this could open a way to inducing and controlling ring-current-related topological phenomena[15].

Within the Bohr model, the electron travels around the nucleus on circular orbits possessing quantized orbital angular momentum associated with a ring current. In quantum mechanics, this motion is reflected by the magnetic quantum number m. In an external magnetic field, the m quantum number becomes observable due to the Zeeman effect, which separates the (initially degenerate) m states in energy. However, this observation of m in the energy domain leaves the underlying circular electron motion invisible. Here we present an ultrafast ionization experiment in which we induce a directional ring current in a ground-state ion by optical tunnelling—a mechanism that impacts atoms and solids in the same way[1]. We probe this ring current in a time-delayed second ionization step, showing how the escaping electron maps its bound-state circular motion onto a detector. In rare gas atoms, such as argon, orbitals of positive and negative m with their clockwise and anticlockwise direction of rotation are equally populated and no net ring current remains. However, if one finds a process that selectively ejects an electron from only one of these energetically degenerate orbitals, then the remaining ion will possess a stationary ring current with defined sign, even in its ground state[16]. For non-vanishing spin–orbit splitting and m-selective tunnel ionization, spin–orbit wavepackets are created that evolve with a period of $T \approx 23.3$ fs for argon that are not resolved in this experiment[17–19]. Similar ground-state currents emerging due to optical tunnelling in condensed-matter systems (for example, in solid argon) could result in topological edge currents in a manner similar to their appearance in twisted waveguides[15], opening an exciting opportunity for ultrafast imaging and control of their formation in condensed-matter systems.

Recent theoretical works predicted that optical tunnelling through a rotating barrier depends on the sign of the magnetic quantum number m[4,7,20,21]. Such a barrier can be created by a strong circularly polarized laser pulse impinging on the atom (Fig. 1). Counter-intuitively, theory predicts that electrons that are counter-rotating with respect to the tunnelling barrier, are strongly preferred for tunnel ionization[4,7,20]. Using this insight, the generation of spin-polarized electrons has been predicted[20] and measured recently[22]. Another experiment demonstrated that sequential double ionization rates by two subsequent circular laser pulses increase if their polarizations are counter-rotating, compared to the case when both rotate in the same direction[23]. In the present work, we directly prove and quantify this quantum-state selectivity of optical tunnelling in a pump–probe experiment. To distinguish emitted electrons with different m, we have employed the following simple idea. Suppose an electron escaping from the tunnel into the continuum keeps its original angular momentum. Then, at the position of the tunnel exit r_t, an angular momentum of $m\hbar$ corresponds classically to a linear momentum of $p_\perp = m\hbar/r_t$ perpendicular to the tunnel direction. Thus, the electron starts its motion in the field with an additional initial momentum. Depending on the sign of m with respect to the direction of rotation of the laser field, this initial momentum either adds to or subtracts from the laser-induced drift momentum. Measuring the momentum distribution should then give direct access to stationary ring currents present in a single atom as well as to the 'transport' of angular momentum through the tunnelling barrier.

In spite of the seeming simplicity of the idea, visualizing these ring currents in an experiment is demanding. Two circularly polarized laser pulses have to be employed. The pump laser pulse should generate the ring current in the ion. To detect this current, we apply a probe laser pulse to remove a second electron that should carry the fingerprint of the current in its energy spectrum. A major challenge in the experiment is to identify the atoms that have been ionized subsequently by the pump and the probe pulse and have not been doubly ionized by either of the two. Accordingly, the properties of the pump and the probe pulses need to differ such that the measured electrons carry information on their ionization sequence.

[1]Institut für Kernphysik, Goethe-Universität Frankfurt am Main, Frankfurt am Main, Germany. [2]Max Planck Institute of Microstructure Physics, Halle (Saale), Germany. [3]Max Born Institute, Berlin, Germany. [4]Technische Universität Berlin, Berlin, Germany. *e-mail: eckart@atom.uni-frankfurt.de; doerner@atom.uni-frankfurt.de

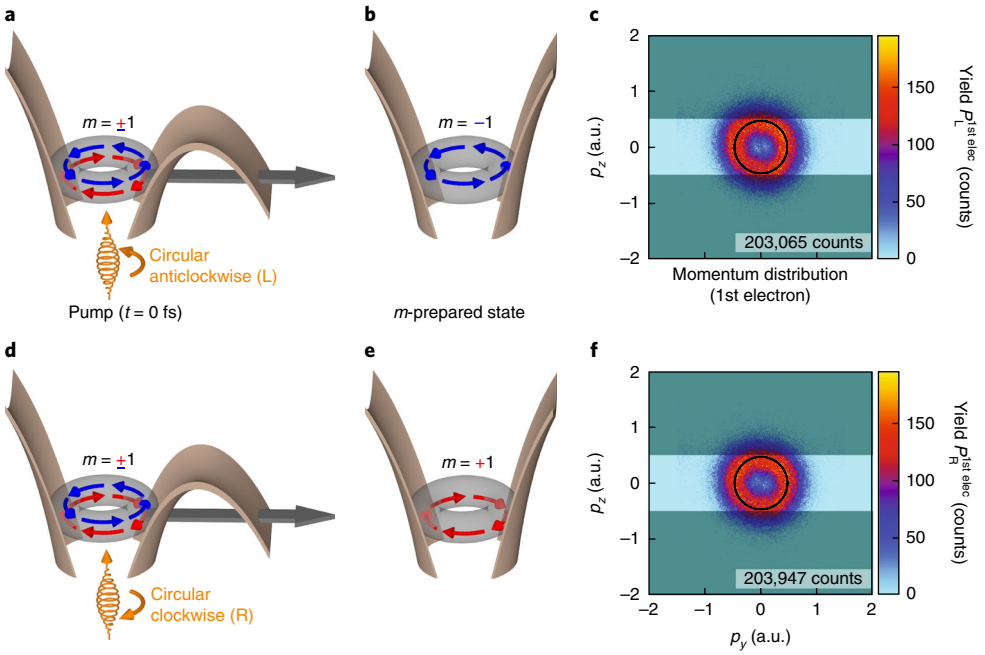

Fig. 1 | Experimental preparation of ring currents by *m*-dependent tunnel-ionization. a, The circularly polarized laser pulse with an anticlockwise-rotating electric field liberates an electron by tunnel-ionization at $t = 0$ fs. Clockwise-rotating electrons ($m = +1$) are strongly preferred for ionization. **b**, Step **a** results in a persistent ring current in the remaining ion. **d**,**e**, The corresponding process for a circular clockwise-rotating electric field. The sign of m and direction of the ring current are inverted. **c**,**f**, Only the pump pulse is used and the electron momentum distributions $P_L^{1st\ elec}$ and $P_R^{1st\ elec}$, showing electrons that are detected in coincidence with Ar^{1+} for equal acquisition times, are identical. The black lines show the negative vector potential of the pump pulse. Most of the first electrons fulfil $|p_z| < 0.5$ a.u. (indicated by the unshaded area), which will be utilized for distinguishing electrons from the pump and the probe pulse. Note that the light propagation direction points out of the paper in **c**,**f**.

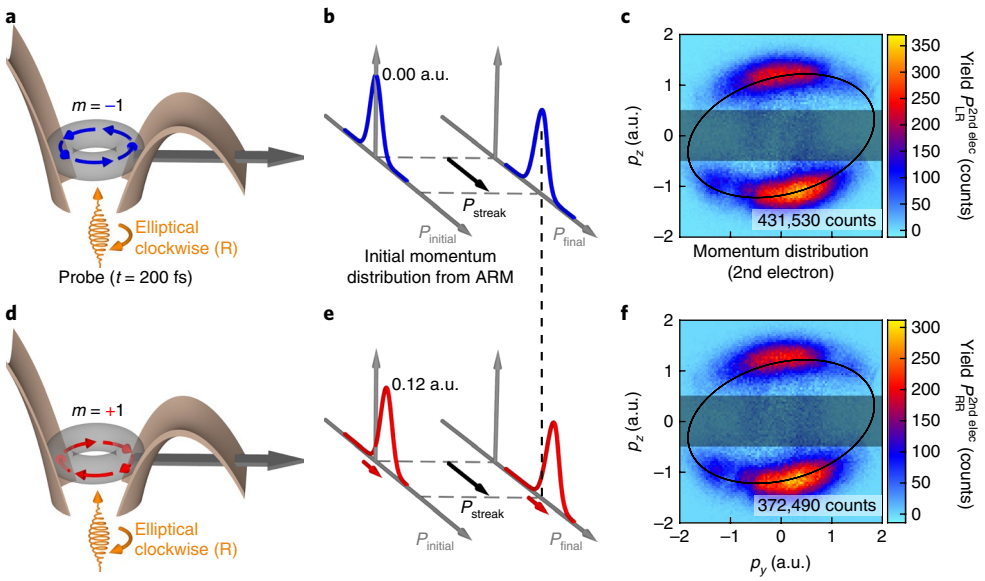

Fig. 2 | Detection of ring currents by momentum-resolved *m*-dependent tunnel-ionization. a,**d**, At $t = 200$ fs, the elliptically polarized probe pulse with a clockwise-rotating electric field hits the ion that has been created by the pump pulse (see Fig. 1). **c**,**f**, The second electron's momentum distributions $P_{LR}^{2nd\ elec}$ and $P_{RR}^{2nd\ elec}$ for equal acquisition times (the electron that is not measured is calculated from momentum conservation and the measured electron is shown in **c, f** only if the calculated electron fulfils $|p_{z\_calc}| < 0.5$ a.u.). The momenta agree with the negative vector potential of the field (black line). There are more events in $P_{LR}^{2nd\ elec}$ than in $P_{RR}^{2nd\ elec}$, proving that the sign of the magnetic quantum number influences tunnel ionization. The angular and radial differences are discussed in Fig. 3 and Supplementary Fig. 3. The electron's 'initial' momentum distributions after tunnelling (dashed line in **b**, **e**) with $m = +1$ have a higher momentum (peak at $p = 0.12$ a.u.) than $m = -1$ (peak at $p = 0.00$ a.u.). These add to the drift momentum imparted by the laser pulse, leading to different final radial momenta (solid lines in **b**,**e**). The transverse offsets for distributions in **b**,**e** are estimated using ARM theory (see text). Note that the light propagation direction points out of the paper in **c**,**f**.

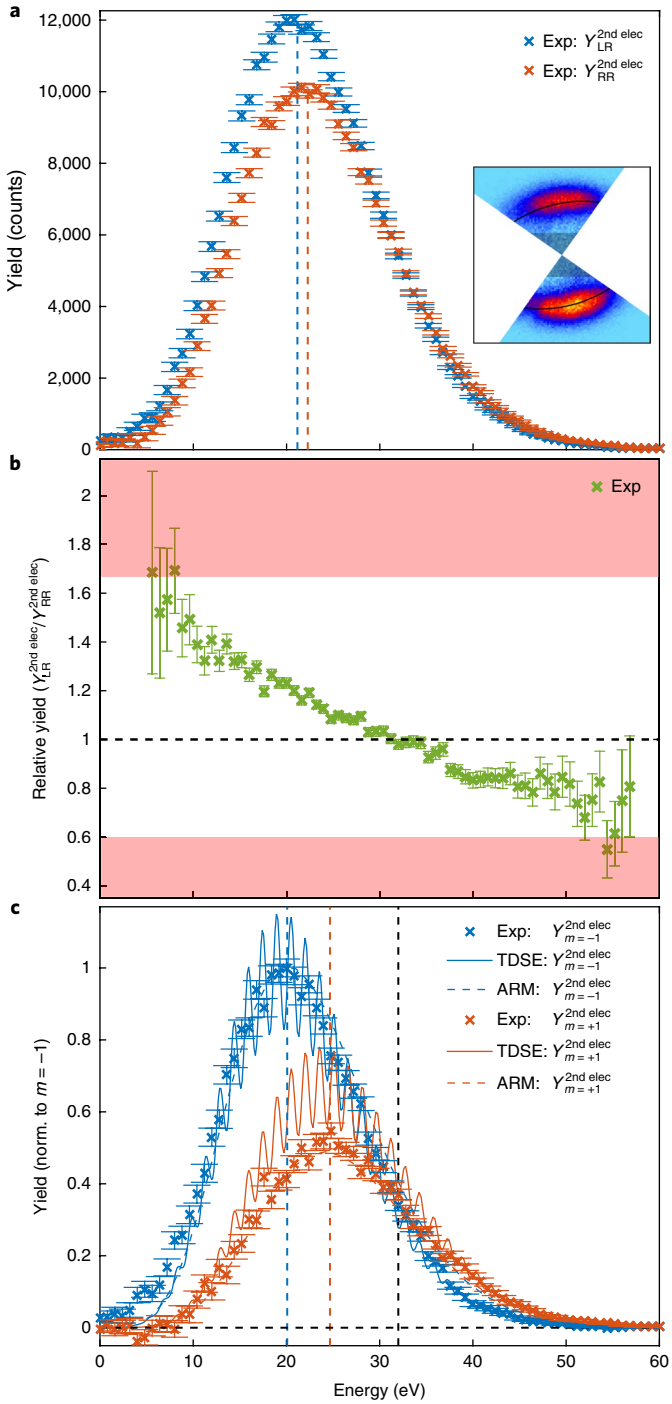

Fig. 3 | Energy-resolved electron spectra showing ring current transport during tunnelling. a, Measured electron energy spectra for $Y_{LR}^{2nd\ elec}$ and $Y_{RR}^{2nd\ elec}$. To reduce noise, the momentum window shown in the inset is applied to the experimental data; the same window is used to gate theoretical and numerical results. **b**, The ratio of ionization rates $\frac{Y_{LR}^{2nd\ elec}}{Y_{RR}^{2nd\ elec}}$ is found to be between 0.6 and 1.67. This asymptotic behaviour for low and high energies can be used to experimentally obtain $Y_{m=-1}^{2nd\ elec}$ and $Y_{m=+1}^{2nd\ elec}$ (see Methods for details). **c**, Energy-dependent yields $Y_{m=-1}^{2nd\ elec}$ and $Y_{m=+1}^{2nd\ elec}$ according to equations (1) and (2) from the Methods are calculated directly from the measured data (squares) and are compared with our theoretical results (ARM theory, dashed lines) and numerical simulations of the time-dependent Schrödinger equation (solid lines) (see Methods). The error bars show the standard deviation of the statistical errors. The maxima are indicated by the vertical coloured lines.

In our pump–probe experiment, a circularly polarized pump pulse with a wavelength of $\lambda = 390$ nm ejects a first electron and a delayed more intense elliptically polarized probe pulse with a wavelength of $\lambda = 780$ nm ejects the second electron from an argon atom. We measure the changes in ionization rate and the momentum distribution of the second electron on switching the helicity of the pump pulse, while the probe pulse remains the same in all cases. Throughout all measurements, the helicity of the pump was inverted every 3 min. Figures 1 (total acquisition time is 3 h and only the pump pulse is used) and 2 (total acquisition time is 35 h and the pump–probe sequence is used) show the pump and probe step in more detail. For $t = 0$ fs, the circularly polarized ultrashort pump pulse with an intensity of $I_0 = 2.1 \times 10^{14}$ W cm^{-2} creates a singly charged argon ion. About 200 fs later, long after the pump pulse is gone, the second electron is emitted from the ion by the probe pulse (ellipticity of 0.61 with a peak electric field of $F_L = 0.11$ a.u., corresponding to an intensity of $I_L = 8.5 \times 10^{14}$ W cm^{-2} for circularly polarized light). Since the liberated electrons are accelerated by the laser field, their final momenta are proportional to $|F_L \times \lambda|$, which is very different for both pulses. Thus, one can tell from the final momentum of each electron whether it was ejected in the pump or in the probe step. Moreover, the coincident detection of electrons and ions allows us to identify and reject events where both electrons are set free by the same pulse, as described in more detail in the Methods.

Figure 1 displays the momentum distributions of the electron emitted by the pump pulse with anticlockwise-rotating polarization (Fig. 1c, indicated by 'L') and clockwise-rotating polarization (Fig. 1f, indicated by 'R'). As both m states are equally populated in the neutral Ar atom, the momentum distributions and ionization rate are independent of the sign of the helicity of the ionizing laser field. However, the memory about the direction of rotation of the ejected electron is recorded in the ion (Figs. 1 and 2a,d). Due to symmetry, the singly ionized states shown in Fig. 1b,e must be mirror symmetric. Will the second ionization step read out this memory? This ability depends on the frequency of the laser field. In the adiabatic tunnelling limit, the barrier does not rotate during tunnelling. Hence, tunnelling from the states with positive and negative m will be identical and the information about the initial direction of the electron's rotation will be lost. The multiphoton ionization regime offers a more optimistic picture: one would expect that the electron escapes with the angular momentum $I_p/\omega + m\hbar$, where I_p/ω is the angular momentum associated with the absorption of the minimal number of photons required to overcome the ionization potential I_p. Hence, in the intermediate, so-called non-adiabatic tunnelling regime[2,3], the difference in the angular momenta Δl_z for the $\pm|m|$ electrons just after tunnelling should be between zero and $2|m|\hbar$ (see Supplementary Figs. 1 and 2 for semiclassical calculations). Our theory, which uses the analytical R-matrix (ARM) method[5,11,24–26] (see Methods), estimates that $\Delta l_z \approx \hbar$ in the conditions of our experiment (Fig. 2b,e). At the tunnel exit r_t, this difference corresponds to different transverse velocities, $\Delta v_\perp = \Delta l_z / r_t$, which translate into the different final momenta at the detector. Figure 2b,e shows how the initial m is transported through the tunnel and mapped onto the final electron spectrum.

We can now investigate the momentum distribution of the second electron $P^{2nd\ elec}$ for two scenarios. The electric field of the probe pulse rotates clockwise in all cases shown here (indicated by 'R'). Figure 2c (respectively, Fig. 2f) shows $P_{LR}^{2nd\ elec}$ (respectively, $P_{RR}^{2nd\ elec}$) for the case where the first electron has been removed by an anticlockwise (respectively, clockwise)-rotating field. While, at first glance, both distributions appear to be similar, detailed examination unveils slight differences, which become prominent in the corresponding angle-integrated kinetic energy spectra $Y^{2nd\ elec}$ of the second electron shown in Fig. 3a (see Supplementary Fig. 3 for two-dimensional differential momentum spectra and Supplementary Fig. 4 and Methods for details about how to distinguish the first

and second electrons). The measured peak energies are 22.3 eV for $Y_{RR}^{2nd\ elec}$ and 21.2 eV for $Y_{LR}^{2nd\ elec}$. This disparity not only signifies the presence of the ring current in the Ar ion, but also allows us to detect its direction, directly observing the propensity rules of the optical tunnelling: the electron counter-rotating to the laser field is preferred, dominating at low energies in the spectra (Fig. 3a,b).

The relative yield $R(E) = Y_{LR}^{2nd\ elec}(E)/Y_{RR}^{2nd\ elec}(E)$ (Fig. 3b) is close to 2 for low-energy electrons, equals 1 at 31.2 eV and drops below unity at high energies. Since there are two electrons for each m state in a p orbital, $R(E)$ must fulfil $0.5 \leq R(E) \leq 2$. The observation that the relative yield is close to 2 for the low-energy electrons allows us to conclude that the pump pulse—depending on its helicity—almost perfectly selects either $m=+1$ or $m=-1$ (see Methods for a refined analysis including correlation effects and a quantum mechanical description of the electron hole). Using this insight, we are able to obtain the energy-dependent yields $Y_{m=-1}^{2nd\ elec}$ and $Y_{m=+1}^{2nd\ elec}$ for $m=-1$ and $m=+1$ electrons (see Fig. 3c). Not only are the absolute yields for $Y_{m=-1}^{2nd\ elec}(E)$ and $Y_{m=+1}^{2nd\ elec}(E)$ different, but also the peaks are shifted in energy by 4.6 eV, in excellent agreement with analytical theory and in good agreement with numerical time-dependent Schrödinger equation simulations.

Our findings demonstrate that the radial shift of the final momentum is a fingerprint of the ring current induced in the ion by optical tunnelling. We have traced this effect back to the m-dependent 'initial' transverse momentum at the tunnel exit. The substantial change of yield and energy of the second electron released by the unmodified probe pulse on inverting the helicity of the pump pulse experimentally proves that the singly charged ion stores information about the helicity of the pump pulse. It also quantifies the transport of angular momentum through the rotating tunnelling barrier. Thus, the often neglected role of the sign of the magnetic quantum number plays a major role in strong-field ionization. We expect that this is not restricted to atoms but will also influence molecular ionization.

Methods

Methods, including statements of data availability and any associated accession codes and references, are available at https://doi.org/10.1038/s41567-018-0080-5.

Received: 12 May 2017; Accepted: 12 February 2018;
Published online: 26 March 2018

References

1. Keldysh, L. V. Ionization in the field of a strong electromagnetic wave. *Sov. Phys. JETP* **20**, 1307–1314 (1965).
2. Ivanov, M., Spanner, M. & Smirnova, O. Anatomy of strong field ionization. *J. Mod. Opt.* **52**, 165–184 (2005).
3. Yudin, G. & Ivanov, M. Nonadiabatic tunnel ionization: Looking inside a laser cycle. *Phys. Rev. A* **64**, 13409 (2001).
4. Barth, I. & Smirnova, O. Nonadiabatic tunneling in circularly polarized laser fields: Physical picture and calculations. *Phys. Rev. A* **84**, 63415 (2011).
5. Kaushal, J. & Smirnova, O. Nonadiabatic Coulomb effects in strong-field ionization in circularly polarized laser fields. *Phys. Rev. A* **88**, 13421 (2013).
6. Zhu, X. et al. Helicity sensitive enhancement of strong-field ionization in circularly polarized laser fields. *Opt. Express* **24**, 4196–4209 (2016).
7. Kaushal, J., Morales, F. & Smirnova, O. Opportunities for detecting ring currents using an attoclock setup. *Phys. Rev. A* **92**, 63405 (2015).
8. Landsman, A. S. & Keller, U. Attosecond science and the tunnelling time problem. *Phys. Rep.* **547**, 1–24 (2015).
9. Shafir, D. et al. Resolving the time when an electron exits a tunnelling barrier. *Nature* **485**, 343–346 (2012).
10. Pedatzur, O. et al. Attosecond tunnelling interferometry. *Nat. Phys.* **11**, 815–819 (2015).
11. Torlina, L. et al. Interpreting attoclock measurements of tunnelling times. *Nat. Phys.* **11**, 503–508 (2015).
12. Garg, M. et al. Multi-petahertz electronic metrology. *Nature* **538**, 359–363 (2016).
13. Eckle, P. et al. Attosecond ionization and tunneling delay time measurements in helium. *Science* **322**, 1525–1529 (2008).
14. Hassan, M. T. et al. Optical attosecond pulses and tracking the nonlinear response of bound electrons. *Nature* **530**, 66–70 (2016).
15. Rechtsman, M. et al. Photonic Floquet topological insulators. *Nature* **496**, 196–200 (2013).
16. Barth, I. & Manz, J. Electric ring currents in atomic orbitals and magnetic fields induced by short intense circularly polarized π laser pulses. *Phys. Rev. A* **75**, 12510 (2007).
17. Fleischer, A. et al. Probing angular correlations in sequential double ionization. *Phys. Rev. Lett.* **107**, 113003 (2011).
18. Fechner, L., Camus, N., Ullrich, J., Pfeifer, T. & Moshammer, R. Strong-field tunneling from a coherent superposition of electronic states. *Phys. Rev. Lett.* **112**, 213001 (2014).
19. Barth, I. & Smirnova, O. Hole dynamics and spin currents after ionization in strong circularly polarized laser fields. *J. Phys. B* **47**, 204020 (2014).
20. Barth, I. & Smirnova, O. Spin-polarized electrons produced by strong-field ionization. *Phys. Rev. A* **88**, 13401 (2013).
21. Li, Y. et al. Nonadiabatic tunnel ionization in strong circularly polarized laser fields: counterintuitive angular shifts in the photoelectron momentum distribution. *Opt. Express* **23**, 28801–28807 (2015).
22. Hartung, A. et al. Electron spin polarization in strong-field ionization of xenon atoms. *Nat. Photon.* **10**, 526–528 (2016).
23. Herath, T., Yan, L., Lee, S. K. & Li, W. Strong-field ionization rate depends on the sign of the magnetic quantum number. *Phys. Rev. Lett.* **109**, 43004 (2012).
24. Torlina, L. & Smirnova, O. Time-dependent analytical R-matrix approach for strong-field dynamics. I. One-electron systems. *Phys. Rev. A* **86**, 43408 (2012).
25. Torlina, L., Kaushal, J. & Smirnova, O. Time-resolving electron-core dynamics during strong-field ionization in circularly polarized fields. *Phys. Rev. A* **88**, 53403 (2013).
26. Torlina, L., Morales, F., Muller, H. G. & Smirnova, O. Ab initio verification of the analytical R-matrix theory for strong field ionization. *J. Phys. B* **47**, 204021 (2014).

Acknowledgements

This work was supported by the DFG Priority Programme 'Quantum Dynamics in Tailored Intense Fields' (projects DO 604/29-1, BA 5623/1-1, IV 156/6-1, SM 292/5-1).

Author contributions

S.E., M.K., M.R., A.H., J.R., F.T., K.F., N.S., K.H., L.Ph.H.S., T.J., M.S. and R.D. contributed to the experiment. S.E., M.K., M.R., K.L., I.B., J.K., F.M., M.I., O.S. and R.D. contributed to the theoretical results. S.E., M.K., T.J., M.S. and R.D. performed the analysis of the experimental data. All authors contributed to the manuscript.

Competing interests

The authors declare no competing interests.

Additional information

Supplementary information is available for this paper at https://doi.org/10.1038/s41567-018-0080-5.

Reprints and permissions information is available at www.nature.com/reprints.

Correspondence and requests for materials should be addressed to S.E. or R.D.

Publisher's note: Springer Nature remains neutral with regard to jurisdictional claims in published maps and institutional affiliations.

Methods

Laser set-up. To generate the two laser pulses, we use a 200 µm β-barium borate crystal to double the frequency of a laser pulse with an initial wavelength of 780 nm (KMLabs Dragon, 40-fs full-width at half-maximum, 8 kHz). A dielectric beamsplitter separates the two pulses of different wavelengths. Subsequently, intensity, polarization state and relative time delay are tuned by neutral-density filters, $\lambda/2$ and $\lambda/4$ retardation plates and a delay stage, respectively. Both laser pulses are focused by a spherical mirror ($f=80$ mm) into a gas target of argon atoms, which is produced by a supersonic expansion of argon gas into the vacuum through a tiny 30 µm nozzle. The gas target was collimated to less than 10 µm along the axial direction in the laser focus to reduce focal averaging. The peak intensities in the focus were calibrated by comparing the measured drift momenta of Ar photoelectrons ionized by the circularly polarized pump pulse with a wavelength of 390 nm to our TDSE calculations. For the intensity calibration of the elliptically polarized probe pulse ($\lambda=780$ nm), a helium target was used to avoid saturation of single ionization. The uncertainty of this calibration method is estimated to be 10%.

Particle detection. On ionization, the fragments are guided by a homogeneous electric field (18.0 V cm^{-1}) and a homogeneous magnetic field (10.4 G) towards time- and position-sensitive detectors. The lengths of the electron and ion arms were 378 mm and 67.8 mm, respectively. The detectors consist of two multi-channel plates in a chevron configuration with a radius of 60 mm and 40 mm for the electron and the ion side, respectively. For both detectors, the multi-channel-plate stack is followed by a three-layer delay-line anode (HEX) with an angle of 60° between layers as manufactured by RoentDek[27]. In this configuration, the three-dimensional momentum of the first electron that hits the detector and one momentum component in the plane of polarization (p_z-direction along time-of-flight) of the ion are measured in coincidence (cold target recoil ion momentum spectroscopy)[28]. The energy resolution of the detected electrons depends on the energy E and is better than 1.3 eV (2.5 eV) for $E<20$ eV ($E<40$ eV). Employing momentum conservation, the undetected electron's momentum component in the time-of-flight direction was calculated (see the following paragraph). Laser, optics set-up and particle detection are the same as used in ref. [29].

Distinguishing electrons emitted by the pump and the probe step in momentum space and background subtraction. The undetected electron's momentum component in the z-direction p_{z_calc} is inferred using momentum conservation. (Note that the electron's momentum component in the x-direction and y-direction cannot be inferred because the momentum resolution on the ion is not sufficient in those directions.) Electrons emitted by the pump pulse have lower momenta (Fig. 1c,f) in the p_z-direction than those generated by the probe pulse (Fig. 2c,f). Imposing the condition $|p_{z\_\mathrm{calc}}|<0.5$ a.u. for the calculated electron, we make sure that the electron that has been detected originates from the ion that was successfully ionized by the pump pulse before. The measured electrons for this condition are seen in Fig. 2. Since the electron momentum distribution is close to the negative vector potential of the probe pulse, we know that those electrons stem from ionization by the probe pulse. See also Supplementary Fig. 4, which shows the electron momentum distributions measured in coincidence with Ar^{2+} without any condition on the detected electron for the cases of pump pulse alone, probe pulse alone and pump and probe pulse. For the spectra shown in Figs. 2 and 3 and Supplementary Figs. 1–3, we have subtracted 35% of the random coincidences.

Obtain experimental spectra for ionization from $m=+1$ or $m=-1$ electrons. Let w^+ (w^-) be the probability of liberating the electron co-rotating (counter-rotating) with the pump pulse. Consider first the case in which the pump and the probe pulses rotate in the same direction. Since there are two electrons for each m state in a p orbital, the amount of counter-rotating electrons available for the second step is $N^-=1+\frac{w^+}{w^++w^-}=1+a$. Here, a is the relative chance of removing a co-rotating electron at the pump step (with $a\in[0,1]$). Thus, the parameter a determines the purity of the state prepared by the pump pulse with $a=0$ being equivalent to perfect selection of a given m state by the pump pulse. The amount of co-rotating electrons available for the second ionization step is $N^+=1+\frac{w^-}{w^++w^-}=2-a$.

In the following, we include two correction factors (Q and C) in our model that can be combined into one correction factor $K=Q\times C$. The factor Q (with $Q>1$) accounts for `hole refilling' (see the section entitled Quantum mechanical description of the created electron hole) and C accounts for correlation effects. The ionization of two electrons with equal magnetic quantum number results in an exited state of Ar^{2+} (^{1}D state), whereas the ionization of two electrons with non-equal magnetic quantum number can lead to the ground state (^{3}P state) or an excited state (^{1}D state) of Ar^{2+}. Since the final states ^{3}P and ^{1}D differ in energy by about 1.74 eV, we cannot assume equal ionization probabilities and include the factor C (with $C>0$) that accounts for correlation effects. $C=1$ would indicate that correlation effects due to the different final states can be neglected and $C=0$ would indicate that it is impossible to sequentially ionize two electrons with equal magnetic quantum number. Finally, the photoelectron signal generated by the probe pulse in the co-rotating set-up follows by summing up all contributing channels:

$$\begin{aligned} Y_{\mathrm{RR}}^{\mathrm{2nd\ elec}}(E) &= [(1-a_{\mathrm{TH}})K+2a_{\mathrm{TH}}]\,Y_{m=-1}^{\mathrm{2nd\ elec}}(E) \\ &+ [2(1-a_{\mathrm{TH}})+a_{\mathrm{TH}}K]\,Y_{m=+1}^{\mathrm{2nd\ elec}}(E) \end{aligned} \quad (1)$$

where $Y_{m=\pm1}^{\mathrm{2nd\ elec}}(E)$ describe photoelectron yields for the probe step. Similarly, for the counter-rotating set-up:

$$\begin{aligned} Y_{\mathrm{LR}}^{\mathrm{2nd\ elec}}(E) &= [(1-a_{\mathrm{TH}})K+2a_{\mathrm{TH}}]\,Y_{m=+1}^{\mathrm{2nd\ elec}}(E) \\ &+ [2(1-a_{\mathrm{TH}})+a_{\mathrm{TH}}K]\,Y_{m=-1}^{\mathrm{2nd\ elec}}(E) \end{aligned} \quad (2)$$

We assume that for high energies only $Y_{m=+1}^{\mathrm{2nd\ elec}}(E)$ contributes because $Y_{\mathrm{LR}}^{\mathrm{2nd\ elec}}(E)$ and $Y_{\mathrm{RR}}^{\mathrm{2nd\ elec}}(E)$ have different peak energies, which explains the pronounced energy difference in Fig. 3b. Then, the relative yield $R(E)=Y_{\mathrm{LR}}^{\mathrm{2nd\ elec}}(E)/Y_{\mathrm{RR}}^{\mathrm{2nd\ elec}}(E)$ for high energies fulfils:

$$R_{\mathrm{highE}}=\frac{2a_{\mathrm{TH}}+(1-a_{\mathrm{TH}})K}{2(1-a_{\mathrm{TH}})+a_{\mathrm{TH}}K} \quad (3)$$

It can be shown that the ratio must be inverse for low energies. The experimental relative yield from $Y_{\mathrm{LR}}^{\mathrm{2nd\ elec}}$ and $Y_{\mathrm{RR}}^{\mathrm{2nd\ elec}}$ (Fig. 3b) reaches values close to $R_{\mathrm{highE}}=0.6\pm0.1$ for high-energy electrons (the limits are marked in Fig. 3b). From the numerical TDSE simulations regarding the pump step, we know that $a_{\mathrm{TH}}\approx0.12$. This allows us to determine K:

$$K=2\frac{a_{\mathrm{TH}}+a_{\mathrm{TH}}R_{\mathrm{highE}}-R_{\mathrm{highE}}}{R_{\mathrm{highE}}a_{\mathrm{TH}}+a_{\mathrm{TH}}-1}\ =\ 1.01\pm0.17 \quad (4)$$

The value of K is close to one (correlation effects and hole refilling cancel each other, with $C=0.83\pm0.14$ and $Q=\frac{11}{9}$). Setting $a_{\mathrm{TH}}=0.12$ and $K=1.01$ in equations (1) and (2), we obtain the experimental energy-dependent yields $Y_{m=-1}^{\mathrm{2nd\ elec}}$ and $Y_{m=+1}^{\mathrm{2nd\ elec}}$ for $m=-1$ and $m=+1$ electrons (see Fig. 3c). Different values for a_{TH} lead to different values of K but it can be shown that the experimentally obtained yields $Y_{m=-1}^{\mathrm{2nd\ elec}}$ and $Y_{m=+1}^{\mathrm{2nd\ elec}}$ are independent of the choice of a_{TH} and depend only on the experimental value R_{highE}.

Quantum mechanical description of the created electron hole. On ionization, the electron hole density in the remaining ion oscillates with the frequency ω_{SO} due to spin–orbit splitting[19,30]. For the case of ejection of a spin-up electron with $m=-1$, the resulting hole is time-independent since its total angular momentum can only be $J=3/2$:

$$W_{m=-1(\mathrm{spin\ down})}=1\times\frac{1}{2} \quad (5)$$

The multiplication by $\frac{1}{2}$ reflects that the chance of making a spin-down hole is 50%, which is equal to that of making a spin-up hole. On ionization of a spin-down electron, the created electron hole is a superposition of an electron hole with a total angular momentum of $J=\frac{3}{2}$ and $J=\frac{1}{2}$. Therefore, the electron hole oscillates between $m=-1$ (spin-up) and $m=0$ (spin-down). The population of the $m=-1$ (spin-up) electron hole state as a function of time t is[19]:

$$W_{m=-1(\mathrm{spin\ up})}(t)=[5/9+4/9\ \cos(\omega_{\mathrm{SO}}t)]\times\frac{1}{2} \quad (6)$$

The multiplication by $\frac{1}{2}$ here also reflects the fact that there is a 50% chance of making a spin-up hole. In the experiment, the pump and the probe pulse are substantially longer than the period of spin–orbit splitting ($T\approx23.3$ fs). (A dependence on the pump–probe delay would only be observable for short pulses and perfect coherence of the electron hole that is created by the pump pulse.) As a result, the oscillation vanishes, leading to the following effective population of the $m=-1$ electron hole, (unresolved on the spin):

$$<W_{m=-1}>\ =1\times\frac{1}{2}+\frac{5}{9}\times\frac{1}{2}=\frac{7}{9} \quad (7)$$

This value deviates from unity, indicating that due to the conversion of electron holes with $m=-1$ (spin-up) to electron holes with $m=0$ (spin-down), the electron hole with $m=-1$ is expected to be refilled by $\frac{2}{9}$ of an electron hole. The exact same derivation holds true for a hole created with $m=+1$, leading to an oscillating electron hole between $m=+1$ (spin-down) and $m=0$ (spin-up). (Ionization of the $m=0$ state by the circularly polarized probe field is negligible due to symmetry.) For the experiment, this means that any hole that is created in the pump step is refilled with $\frac{2}{9}$ electrons, leading to an available number of $1+\frac{2}{9}$ electrons instead of exactly 1 electron with the given magnetic quantum number. The scalar value $Q=\frac{11}{9}$ is used to describe this effect ('hole refilling') in our experiment. Since

© 2018 Macmillan Publishers Limited, part of Springer Nature. All rights reserved.

'hole refilling' affects only the scenarios in which the pump and probe subsequently ionize an electron with the same magnetic quantum number, the scalar value of Q appears as a factor together with the scalar value C (accounting for correlation effects) since the correlation effect is relevant for the same channels.

Numerical time-dependent Schrödinger equation simulations. Our numerical simulations are based on solving the time-dependent Schrödinger equation (TDSE) first for the pump step and then for the probe step, assuming sequential ionization. In both cases, a single active electron moves in an effective potential. For the pump step, two different effective potentials have been used, one developed and verified in refs [31,32] $V_{1,\mathrm{Ar}}(r) = -(1. + 5.4\ \exp(-r) + 11.6\ \exp(-3.682r))/r$, and another defined as $V_{2,\mathrm{Ar}}(r) = -[1 + 17\ \exp(-r^2/1.1364)]/\sqrt{r^2 + 0.997\ \exp(-2r^2)}$, both adjusted to fit the ionization potential of argon from the p shell. The numerical method used was described in refs [31,32] and is identical to that employed by us in refs [11,22,26]. For the pump step, only energy-integrated relative ionization yield from the co-rotating and counter-rotating orbitals is needed. For the estimated pump intensity (carrier frequency of $\omega = 0.114$ a.u., field strength $F = 0.055$ a.u.), the ratio $a = w^+/(w^+ + w^-)$ was found to be $a = 0.18$ and $a = 0.12$ for the first and the second potential respectively, demonstrating predominant ionization from the orbital counter-rotating to the pump field. For the probe step, the results shown in Fig. 3 and Supplementary Fig. 3 used $V_{3,\mathrm{Ar}^+}(r) = -2/r + \mathrm{U}(r)$, with the short-range part $U(r) = -6.24\ \exp(-1.235 \times r)/r$ adjusted so that the binding energy of the first p state is equal to the ionization potential of Ar^+ ($I_p = 1.0153$ a.u.), and the next excited s state ($E = -0.3845$ a.u.) approximates the first excitation in the Ar^+ ion. The calculations were performed for the orbitals co- and counter-rotating with respect to the probe field.

The pulses used to produce the TDSE results in Fig. 3 and Supplementary Fig. 3 had carrier frequency $\omega = 0.057$ a.u., a $\cos^4(\pi t/NT)$ intensity envelope, with a full duration of $N = 6$ optical cycles $T = 2\pi/\omega$ (base to base). The pulses have an ellipticity $\epsilon = 0.61$, with $F_z = \epsilon F_y$. We have performed calculations for six intensities with $0.09 \le F_y \le 0.115$ a.u. in steps of $\Delta F_y = 0.005$ a.u. The results of the simulations were averaged over the carrier envelope phase (CEP) of the pulse, incremented in steps of $\Delta CEP = 0.05\pi$. The results were also averaged over the focal volume intensity distribution, assuming Gaussian focus and that the gas jet was much thinner than the length of the focal spot. The same procedure was used for the analytical R-matrix (ARM) calculations described below. The ARM and the TDSE results presented in Figs. 2 and 3 and Supplementary Fig. 3 use $F_y = 0.11$ a.u. as the peak field strength.

The discretization box used for the simulations had a radial box size of 1,000 a.u., with $\Delta r = 0.1$ a.u. The maximum angular momentum included is $l_{\max} = 160$, and the time step was $\Delta t = 0.036$ a.u. A complex boundary absorber was placed starting at 30 a.u. before the end of the simulation volume to avoid unwanted reflections from the boundaries. The convergence of the numerical calculations has been checked with respect to all discretization parameters. The photoelectron spectra were calculated by propagating the wavefunction one extra cycle after the end of the pulse, and applying a spatial mask with a radius of 75 a.u. to remove the bound part of the wavefunction. The remaining (continuum) part was then projected on the well-known exact continuum eigenstates of the doubly charged Coulomb centre. The accuracy of this procedure has been monitored by varying the extra propagation time up to five cycles, and by varying the radius and the width of the spatial mask.

To compare with the experimental measurements, in Fig. 3c, we have used an angular filter, in the same way as in the experiment, imposing two 90-degree integration windows, centred at 100 degrees and 180 + 100 degrees respectively.

Analytical R-matrix theory. The analytical R-matrix (ARM) approach has been described in detail in refs [5,7,11,24–26], with ref. [7] focusing on its application to strong-field ionization from orbitals with non-zero l,m. The ARM method yields the following expressions for the photoelectron signal at the momentum $\mathbf{p}$

$$|a(\mathbf{p})|^2 = |R_{l,m}(\mathbf{p})|^2\ \mathrm{e}^{2\mathrm{Im}S(\mathbf{p},t_s)} \tag{8}$$

The second term encodes the bulk of the 'weight' of the quantum trajectory defined by the initial coordinate (at the origin) and the final momentum $\mathbf{p}$ at the detector. The trajectory leaves the bound orbital at a complex-valued time $t_s = t_s(\mathbf{p})$ and moves according to the Newton equations, both in the classically forbidden and classically allowed regions. Extension into the classically forbidden region makes the starting time $t_s = t_s(\mathbf{p})$ complex-valued. The time $t_s = t_s(\mathbf{p})$ is found as the solution of $\partial S(\mathbf{p},t)/\partial t = 0$, where the action $S(\mathbf{p},t_s)$ is calculated along the complex-valued trajectory and is complex-valued. The strength of the photoelectron signal depends on its (negative) imaginary part $\mathrm{Im}S(\mathbf{p},t_s)$. The action includes the electron interaction with the laser field and the core potential. Further details are briefly summarized in equations (2)–(6) of the Supplementary Information of ref. [11], with complete mathematical treatment presented in refs [5,7,24–26], including the verification against ab initio simulations of the time-dependent Schrödinger equation (5).

The first term in equation (8) encodes the angular structure of the ionizing orbital, $R_{lm}(\mathbf{p}) \propto \mathrm{e}^{\mathrm{Im}\varphi(\mathbf{p})}$, where $\varphi(\mathbf{p})$ is the complex-valued 'tunnelling' angle—the angle at which the trajectory leaves the origin, $\tan\varphi(\mathbf{p}) = v_y(t_s(\mathbf{p}))/v_x(t_s(\mathbf{p}))$. The angle is complex-valued due to the complexity of the velocity in the classically forbidden region, and its imaginary part determines the relative ionization yields from orbitals with $m = \pm|m|$: $|R_{l,+|m|}(\mathbf{p})|^2/|R_{l,-|m|}(\mathbf{p})|^2 \propto \mathrm{e}^{-4|m|\mathrm{Im}\varphi(\mathbf{p})}$. The effects of the core potential on the outgoing electron are included in the action and in the shift of the ionization time $t_s = t_s(\mathbf{p})$. The corrections to the tunnelling angle $\varphi(\mathbf{p})$ associated with the effect of the core potential were not included.

Semiclassical calculation. The semiclassical simulation of ionization for the argon ion by the 780 nm probe pulse is based on the semiclassical two-step model of ref. [33]. The initial conditions (ionization time and transverse momentum) for each trajectory are prepared using importance sampling[33] according to the Ammosov–Delone–Krainov ionization theory[34]. The tunnel exit is obtained in the same way as in ref. [35]. A linear offset momentum $p_\perp = m\hbar/r_t$ in the plane of polarization and perpendicular to the tunnelling direction is added to the momentum distribution. The momentum $p_\perp$ corresponds to an angular momentum of $m\hbar$ at the position of the tunnel exit r_t. The results from our ARM calculation on the transverse momentum distribution at the tunnel exit shown in Fig. 2b,e show a momentum difference of only 0.12 a.u. between the ionization of $m = +1$ and $m = -1$, which is about a factor of two smaller than the value we assume here based on the classical estimate $p_\perp = m\hbar/r_t$. After tunnelling, an electron is propagated classically in the presence of the doubly charged ionic core and the strong laser field. The analogue of the quantum mechanical phase was calculated from classical action for each final momentum. A peak electric field of $F_{y\_\mathrm{classical}} = 0.114$ a.u. and an ellipticity of $\epsilon = 0.61$ ($F_{z_{\mathrm{classical}}} = \epsilon F_{y_{\mathrm{classical}}}$) have been used. The yields from the semiclassical simulations in Supplementary Figs. 1 and 2 have been normalized to fit the maximum of the experimental data for $m = -1$ and $m = +1$ respectively.

Differences in angle-resolved photoelectron spectra. The photoelectron spectra in Fig. 2c,f also show—besides the discussed radial differences—angular deviations. Those are due to the Coulomb attraction of the outgoing electron to the ionic core. The different `initial conditions' map onto different angular offsets in the final angle-resolved photoelectron spectra originating from $m = +1$ and $m = -1$ states[7], similar to the so-called attoclock set-up[8,13,36,37]. In our experiment, this directly translates (see equations (1) and (2)) into different angular structures in $P_{\mathrm{LR}}^{\mathrm{2nd\ elec}}$ and $P_{\mathrm{RR}}^{\mathrm{2nd\ elec}}$ (see Supplementary Fig. 3 for the differential histograms). Note that, from equations (1) and (2), it can be shown that for each momentum $\mathbf{p}$ in the plane of polarization

$$\begin{aligned}&(P_{m=-1}^{\mathrm{2nd\ elec}}(\mathbf{p}) - P_{m=+1}^{\mathrm{2nd\ elec}}(\mathbf{p})) \times (2a_{\mathrm{TH}}K - 4a_{\mathrm{TH}} - K + 2)\\ &= P_{\mathrm{LR}}^{\mathrm{2nd\ elec}}(\mathbf{p}) - P_{\mathrm{RR}}^{\mathrm{2nd\ elec}}(\mathbf{p})\end{aligned} \tag{9}$$

which indicates that after normalization the differential electron momentum distributions $P_{\mathrm{LR}}^{\mathrm{2nd\ elec}} - P_{\mathrm{RR}}^{\mathrm{2nd\ elec}}$ and $P_{m=-1}^{\mathrm{2nd\ elec}} - P_{m=+1}^{\mathrm{2nd\ elec}}$ are identical.

The additional angular offset associated with the angular momentum of the ionizing state directly affects the interpretation of attosecond measurements of tunnelling dynamics via the attoclock set-up[37] and also extends attoclock-type measurements[8,13,36,37] to multi-cycle laser pulses.

Accordingly, our findings give a purely experimental answer to the lively debated question regarding the role of non-adiabatic electron dynamics during optical tunnelling[8,11]. So far, these effects have been addressed only by comparing experimental observations with calculated ones, using theoretical models to reconstruct the underlying dynamics[8–10,13,36–39].

Data availability. The data that support the findings of this study are available from the corresponding author upon reasonable request.

References

27. Jagutzki, O. et al. Multiple hit readout of a microchannel plate detector with a three-layer delay-line anode. *IEEE Trans. Nucl. Sci.* **49**, 2477–2483 (2002).
28. Ullrich, J. et al. Recoil-ion and electron momentum spectroscopy: reaction-microscopes. *Rep. Prog. Phys.* **66**, 1463–1545 (2003).
29. Eckart, S. et al. Nonsequential double ionization by counterrotating circularly polarized two-color laser fields. *Phys. Rev. Lett.* **117**, 133202 (2016).
30. Pfeiffer, A. N. et al. Calculation of valence electron motion induced by sequential strong-field ionisation. *Mol. Phys.* **111**, 2283–2291 (2013).
31. Nandor, M. J., Walker, M. A., Van Woerkom, L. D. & Muller, H. G. Detailed comparison of above-threshold-ionization spectra from accurate numerical integrations and high-resolution measurements. *Phys. Rev. A* **60**, R1771–R1774 (1999).
32. Muller, H. G. An efficient propagation scheme for the time-dependent Schrodinger equation in the velocity gauge. *Laser Phys.* **9**, 138–148 (1999).
33. Shvetsov-Shilovski, N. I. et al. Semiclassical two-step model for strong-field ionization. *Phys. Rev. A* **94**, 13415 (2016).
34. Delone, N. B. & Krainov, V. P. Energy and angular electron spectra for the tunnel ionization of atoms by strong low-frequency radiation. *J. Opt. Soc. Am. B* **8**, 1207–1211 (1991).

© 2018 Macmillan Publishers Limited, part of Springer Nature. All rights reserved.

35. Lemell, C. et al. Low-energy peak structure in strong-field ionization by midinfrared laser pulses: Two-dimensional focusing by the atomic potential. *Phys. Rev. A* **85**, 11403 (2012).
36. Eckle, P. et al. Attosecond angular streaking. *Nat. Phys.* **4**, 565–570 (2008).
37. Pfeiffer, A. N. et al. Attoclock reveals natural coordinates of the laser-induced tunnelling current flow in atoms. *Nat. Phys.* **8**, 76–80 (2012).
38. Bruner, B. D. et al. Multidimensional high harmonic spectroscopy of polyatomic molecules: detecting sub-cycle laser-driven hole dynamics upon ionization in strong mid-IR laser fields. *Faraday Discuss.* **194**, 369–405 (2016).
39. Torlina, L. & Smirnova, O. Coulomb time delays in high harmonic generation. *New J. Phys.* **19**, 23012 (2017).

© 2018 Macmillan Publishers Limited, part of Springer Nature. All rights reserved.